Phase separation and electrical switching between two isosymmetric multiferroic phases in tensile strained BiFeO₃ thin films

Jin Hong Lee,[1] Kanghyun Chu,[1] Ahmet A. Ünal,[2] Sergio Valencia,[2] Florian Kronast,[2] Stefan Kowarik,[3] Jan Seidel,[4] and Chan-Ho Yang[1,5,*]

[1]*Department of Physics, KAIST, Yuseong-gu, Daejeon 305-701, Republic of Korea*
[2]*Helmholtz Zentrum Berlin, Elektronenspeicherring BESSY II, Albert-Einstein-Strasse 15, D-12489 Berlin, Germany*
[3]*Institut für Physik, Humboldt-Universität zu Berlin, Newtonstrasse 15, D-12489 Berlin, Germany*
[4]*School of Materials Science and Engineering, University of New South Wales, Sydney, New South Wales 2052, Australia*
[5]*KAIST Institute for the NanoCentury, KAIST, Yuseong-gu, Daejeon 305-701, Republic of Korea*

Phase separation of two different isosymmetric phases can occur as a result of their similar ground state energies. We have found such phase separation in a multiferroic system at a tensile-strain-driven morphotropic phase boundary of rhombohedral and orthorhombic bismuth ferrite. We utilize the emergent phase competition in order to implement three-step electric switching of ferroelectric polarization as well as rotation of the magnetic easy axis using electric fields. This observation provides a pathway to phase-competition-driven magnetoelectric devices.

Multiferroics, which refers to compounds with at least two coexisting order parameters such as ferroelectric, ferroelastic, and magnetic order, have been a central topic of condensed matter physics because of intriguing physics of intercoupled phenomena and their potential applications for magnetoelectric devices [1–5]. Bismuth ferrite, BiFeO₃ (BFO), has been extensively studied due to a coexistence of ferroelectric and antiferromagnetic order at room temperature [3]. Bulk BFO (pseudocubic lattice parameter, $a_{pc} \sim 3.965$ Å) has a rhombohedral structure (space group $R3c$) with an electric polarization of $\sim 90~\mu$C/cm² along $\langle 111 \rangle$ [6,7]. Epitaxial films of BFO grown on SrTiO₃ ($a \sim 3.905$ Å) undergo heteroepitaxial distortion leading to a rhombohedral-like monoclinic structure (R-BFO) [8,9]. Moreover, assisted by theoretical studies on the strain-dependent phase diagram of BFO [10,11], it has been found that growth on substrates with widely differing lattice parameters gives rise to the emergence of other isosymmetric phases, i.e., tetragonal-like BFO (T-BFO) [12–19] and orthorhombic BFO (O-BFO) [20–22]. The T-BFO phase is stabilized when BFO is grown on such substrates with smaller lattice parameters as LaAlO₃ ($a_{pc} \sim 3.789$ Å). Remarkably, a strain-driven morphotropic phase boundary has been discovered as a consequence of phase competition between T-BFO and R-BFO [13], which brings about many interesting phenomena such as colossal electrostrain [23,24], interfacial magnetism [25], and electronic conduction [26]. However, phase competition between R-BFO and O-BFO in the regime of tensile strain has not been addressed in detail, despite the importance of a strain-driven morphotropic phase boundary as another counterpart in phase space, which offers new ways to achieve electric-field control of magnetism [20,21,27].

In this Rapid Communication, we report that phase separation of the two competing R-BFO and O-BFO phases occurs in BFO films grown on $(110)_{pc}$-oriented GdScO₃ (GSO;

$a_{pc} \sim 4.014$ Å) substrates. We observe that needle-shaped O-BFO regions form within the R-BFO matrix in as-grown films and that their areal fraction along with ferroelectric polarization is controlled by an external electric field. Remarkably, we observe that poling an area by applying electric fields of moderate strength induces the expansion of O-BFO phase regions. Strong electric fields, however, produce R-BFO dominant states. Furthermore, we determine the magnetic easy axis of O-BFO and R-BFO in this tensile strained case through Fe L-edge x-ray absorption spectromicroscopy. These observations open the door to versatile physics related to the instability at phase boundaries and a conceptual three-step and/or magnetoelectric data storage memory based on phase separation.

Epitaxial BFO thin films were grown on $(110)_{pc}$-oriented GSO substrates with a $\sim$1-nm-thick SrRuO₃ buffer layer by means of pulsed laser deposition (PLD). The GSO substrate has an orthorhombic structure with $a = 5.7454$ Å, $b = 7.9314$ Å, and $c = 5.4805$ Å [28]. The $[110]_{pc}$ pseudocubic direction of the substrate corresponds to the $[001]_o$ orthorhombic direction. Substrate temperature and oxygen pressure were maintained at 700 °C and 100 mTorr during the deposition. A KrF excimer laser ($\lambda = 248$ nm) was operated at the repetition rate of 10 Hz and the laser fluence was adjusted to be $\sim$1 J/cm². For the investigation on crystal structures, a θ-2θ scan and reciprocal space maps (RSMs) were carried out by an x-ray diffractometer (PANalytical X'pert MRD PRO) with Cu $K\alpha_1$ radiation. A scanning probe microscopy instrument (Veeco-DI Multimode V equipped with a Nanoscope controller V) was utilized for out-of-plane (OOP) and in-plane (IP) piezoresponse force microscopy (PFM) measurements as well as surface topography measurements. We used Pt-coated Si tips (HQ:NSC35/Pt, MikroMasch) and a PFM-ac voltage of 3 V was applied at a frequency of 9.995 kHz. The tip velocity during measurements was 4 μm/s. X-ray magnetic linear dichroism (XMLD) and photoemission electron microscopy (PEEM) studies were carried out at the UE-49 PGMa beamline of the BESSY II storage ring of the Helmholtz-Zentrum Berlin
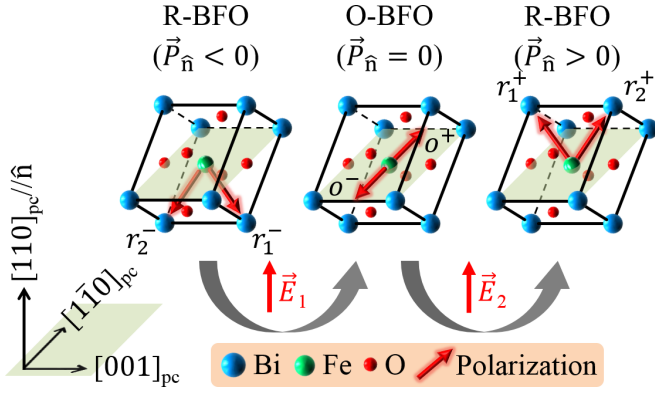
*chyang@kaist.ac.kr

FIG. 1. (Color online) Schematic diagram of electrically switchable R-BFO and O-BFO with possible ferroelectric polarizations in a tensile strained $(110)_{pc}$ BFO thin film on a GSO substrate. To express both ferroelectric and ferroelastic domains simultaneously, we used $r_i^{\pm}$ notation where $i = 1$ or 2 indicates rhombohedral variants and the $+$ or $-$ sign refers to upward or downward polarization. $o^{\pm}$ notation is for orthorhombic variants. $\vec{P}_{\hat{n}}$ denotes the projected ferroelectric polarization along the film normal direction ($\hat{n} \parallel [110]_{pc}$). $\vec{E}_1$ and $\vec{E}_2$ describe the switching fields between R-BFO and O-BFO.

using linearly polarized incident x rays in the region of Fe $L_{2,3}$ edges [29]. The incident x rays with σ polarization (within the sample surface) or π polarization (within a plane perpendicular to the sample surface) were injected at an incident polar angle of 60° from the film normal.

Figure 1 shows a schematic diagram describing possible competing states with their ferroelectric polarizations emerging in a tensile strained $(110)_{pc}$ BFO thin film. The R-BFO phase has a polarization oriented along $\langle 111 \rangle_{pc}$ directions suffering a monoclinic distortion so that the $[110]_{pc}$ axis is slightly tilted toward $[001]_{pc}$. In addition, the ferroelectric polarization of O-BFO in this study lies within the $(110)_{pc}$ plane and thus it does not have any OOP component. We can classify the polarization orientations in the thin film into three groups in terms of OOP polarizations: downward polarization ($\vec{P}_{\hat{n}} < 0$), zero OOP polarization ($\vec{P}_{\hat{n}} = 0$), and upward polarization ($\vec{P}_{\hat{n}} > 0$). We will demonstrate electrical switching between the three states later in this paper.

In order to clarify the purity and strain state of the film, we performed an x-ray θ-2θ scan [Fig. 2(a)] and RSMs around the OOP $(110)_{pc}$ peak and two asymmetric $(221)_{pc}$ and $(210)_{pc}$ peaks [Figs. 2(b) and 2(c)]. No impurity peaks were observed in the θ-2θ scan covering a wide range of 2θ angles. For $(110)_{pc}$ substrates, $[1\bar{1}0]_{pc}$ and $[001]_{pc}$ correspond to two IP directions perpendicular to each other. The longitudinal scan through the GSO $(110)_{pc}$ peak exhibited two BFO peaks indicating the coexistence of two independent phases having different OOP $(110)_{pc}$ lattice parameters. The stronger peak located at a smaller Q_z point is attributed to the R-BFO. The RSM for the $\{221\}_{pc}$ reflections of R-BFO show peak splits along the OOP direction, while the $\{210\}_{pc}$ peaks appear at the expected pseudotetragonal position without any peak splits. These are the characteristic features expected in the monoclinically distorted phase of R-BFO [30]. The double-pseudocubic supercell depicted in Fig. 2(d) has a monoclinic
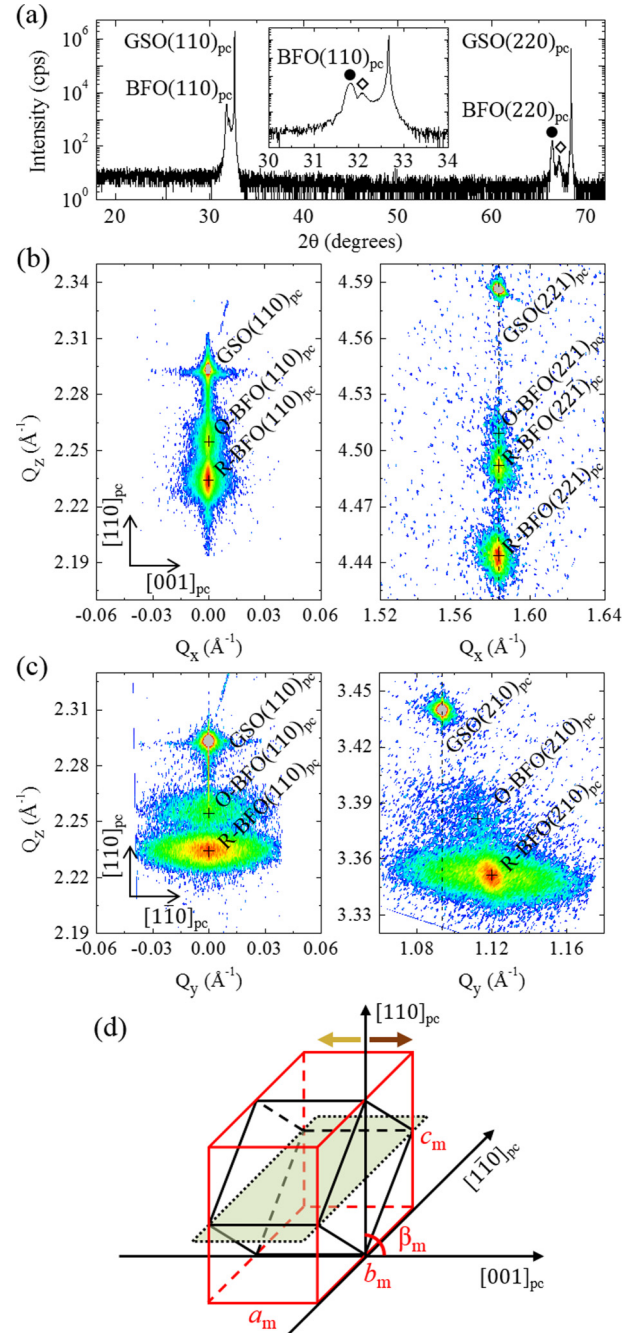

FIG. 2. (Color online) (a) Conventional θ-2θ scan for a BFO film grown on a $(110)_{pc}$ GSO substrate. Circles and diamonds indicate R-BFO peaks and O-BFO peaks, respectively. (b) RSMs for $(110)_{pc}$ and $(221)_{pc}$ peaks with a horizontal reciprocal axis aligned to $[001]_{pc}$. (c) RSMs for $(110)_{pc}$ and $(210)_{pc}$ peaks with a horizontal reciprocal axis aligned to $[1\bar{1}0]_{pc}$. (d) Schematic displaying a monoclinic unit cell (colored red) which has twice larger volume relative to a pseudocubic unit cell (colored black). An olive-colored plane represents the a_m-b_m plane of GSO substrate. The lattice parameters and volumes are determined; $a_m = 3.96(7)$ Å, $b_m = 5.6(5)$ Å, $c_m = 5.57(4)$ Å, $\beta_m = 90.(0)°$, and $V_m = 124.(9)$ Å³ for O-BFO; $a_m = 3.96(7)$ Å, $b_m = 5.61(1)$ Å, $c_m = 5.62(5)$ Å, $\beta_m = 89.1(2)°$, and $V_m = 125.(2)$ Å³ for R-BFO; $a_m = 3.96(7)$ Å, $b_m = 5.74(5)$ Å, $c_m = 5.48(0)$ Å, $\beta_m = 90.0(0)°$, and $V_m = 124.(9)$ Å³ for GSO. We note that all the a_m IP lattice parameters are matched exactly but the other b_m IP parameters are relaxed as a result of uniaxial misfit strain.

distortion so that the OOP direction of $[110]_{pc}$ is tilted toward an IP direction of $[001]_{pc}$ by $\sim 0.9°$, which is due to the fact that the polarizations of R-BFO point to $\langle 111 \rangle_{pc}$. In addition, the asymmetric peaks of O-BFO were detected at the expected pseudotetragonal positions without any splits, indicating that the supercell of O-BFO is orthorhombic. We note that the $(110)_{pc}$ BFO films undergo only uniaxial coherent misfit strain along the $[001]_{pc}$ direction. The horizontal position of $\{221\}_{pc}$ BFO peaks is exactly matched with that of the substrate, however, the $\{210\}_{pc}$ BFO peaks of diffusive shape along the horizontal direction are far away from the IP position of the GSO peak. This is due to the fact that the tensile strained films are partially relaxed along the $[1\bar{1}0]_{pc}$ direction while holding a coherent strain along $[001]_{pc}$. It is considered that the partial strain relaxation plays an important role in phase separation by allowing different IP lattice parameters of the constituent phases. The O-BFO allowing only IP components of polarizations has a larger IP lattice parameter, while the OOP lattice parameter becomes relatively smaller, maintaining the volume that is comparable to that of R-BFO.

In order to investigate the as-grown ferroelectric domain structure of R-O mixed phase thin films, we performed PFM measurements (Fig. 3). As expected, the OOP PFM reveals dark contrast in most areas implying the dominant presence of R-BFO with a downward polarization. Small needle-shaped areas showing no OOP polarization correspond to O-BFO. The possible directions of IP polarization can be demarcated by a single IP-PFM image with a cantilever oriented 45° to the $[001]_{pc}$ crystalline axis. The IP-PFM technique can differentiate the projected IP direction perpendicular to the cantilever orientation. The projected IP polarizations of R-BFO and O-BFO have different magnitudes and thus we can observe two domains (colored yellow and brown) for R-BFO and another two domains (colored white and black) for O-BFO. This PFM measurement clearly confirms phase separation between R-BFO and O-BFO. The BFO film is grown on a conducting $SrRuO_3$ buffer layer and the top surface is exposed to air. The different top/bottom electrostatic boundary condition breaks a mirror symmetry inducing a built-in field preferring the downward polarization in this case. Despite the built-in field, the presence of the O-BFO phase with purely IP directional polarization suggests the O-BFO phase is likely to be the most stable state in the aspect of mechanical deformation energy in such a tensile strained situation.

In the following we discuss the magnetic easy axis ($\vec{M}$) of spin moments for a better understanding of magnetoelectric properties of the compound. The perovskite BFO has $3d^5$ electrons for each Fe^{3+} ion so we expect a G-type antiferromagnetic order indicating all nearest-neighboring spins are aligned in an antiparallel manner according to the superexchange rule [31]. Additionally, the spin-orbit interaction introduces an anisotropic spin-spin interaction defining a magnetic easy axis. Since it is sensitive to the local crystal structure surrounding a corresponding magnetic ion, R-BFO and O-BFO phases are likely to have different magnetic easy axes. To determine the magnetic axes, we carried out x-ray absorption spectroscopy (XAS) across the Fe L edge with a linearly polarized x ray where its electric-field direction ($\vec{E}_{ph}$) is along $[001]_{pc}$ [Fig. 4(a)]. The XAS spectra are divided into L_3 and L_2
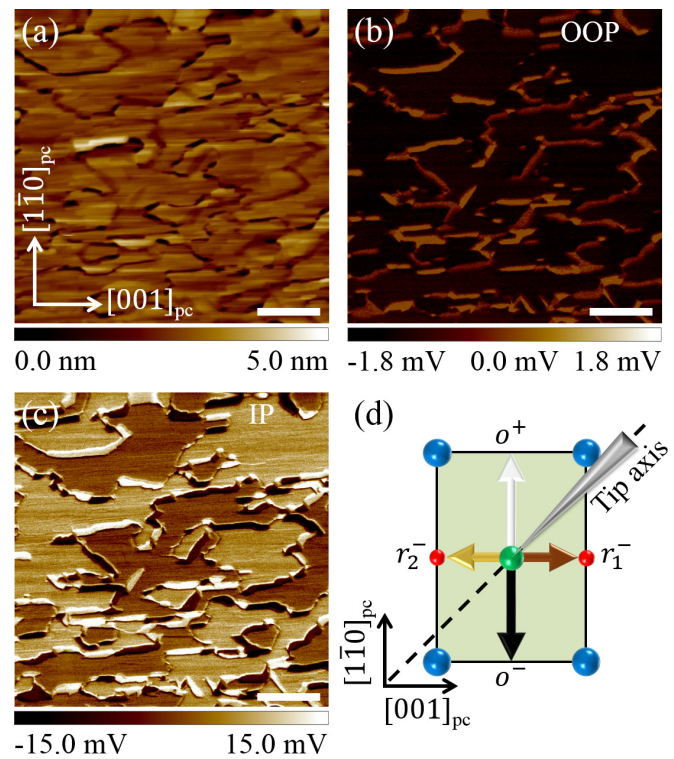

FIG. 3. (Color online) (a) Topographic image of an as-grown $(110)_{pc}$ BFO thin film. Crystal axes are indicated. (b) OOP PFM image exhibiting needle-shaped O-BFO areas with zero OOP polarization (brown, $\vec{P}_{\hat{n}} = 0$) surrounded by the matrix areas of R-BFO with downward polarization (black, $\vec{P}_{\hat{n}} < 0$). (c) IP-PFM real part image discriminating downward polarization ($\vec{P}_{\hat{n}} < 0$) regions including r_1^- (brown) and r_2^- (yellow) domains and zero OOP polarization ($\vec{P}_{\hat{n}} = 0$) regions including o^+ (white) and o^- (black) domains. Scale bars represent 1 μm. (d) Schematic diagram of IP component ferroelectric polarizations for the R-BFO and O-BFO phases. A PFM tip along the black dashed line depicts the fast scan direction oriented 45° to the crystalline $[001]_{pc}$ axis.

peaks due to the $2p$ core hole spin-orbit splitting. Each peak additionally splits into two subpeaks separated by ~ 1.5 eV reflecting the splitting of empty d orbital levels of Fe^{3+} ($3d^5$) into t_{2g} and e_g levels due to the cubic crystal field [32]. The Fe L-edge XAS spectra depend on whether the x-ray polarization is parallel or perpendicular to crystalline or magnetic axes. In the present experiment, the two phases we analyze are located in the same film and their crystalline axes are exactly aligned with each other. Since R-BFO and O-BFO are nearly the same perovskites with only slight differences in lattice parameters of less than 1%, we reasonably assume that the crystal structural effect on XAS is not a dominant factor for such isosymmetric phases. Accordingly, the different feature in the relative strength of two L_2 subpeaks (A and B), as presented in the inset of Fig. 4(a), reflects any discrepancy in the antiferromagnetic axes of O-BFO and R-BFO. Arenholz *et al.* studied systematically the anisotropic nature of XMLD of iron oxides for various experimental geometries [33]. For an experimental geometry where $\vec{E}_{ph}$ is parallel to the Fe-O bond axes of the FeO_6 octahedron, e.g., $\langle 100 \rangle_{pc}$ axes of perovskites, the intensity of subpeak B (I_B) at 722.5 eV [that of subpeak
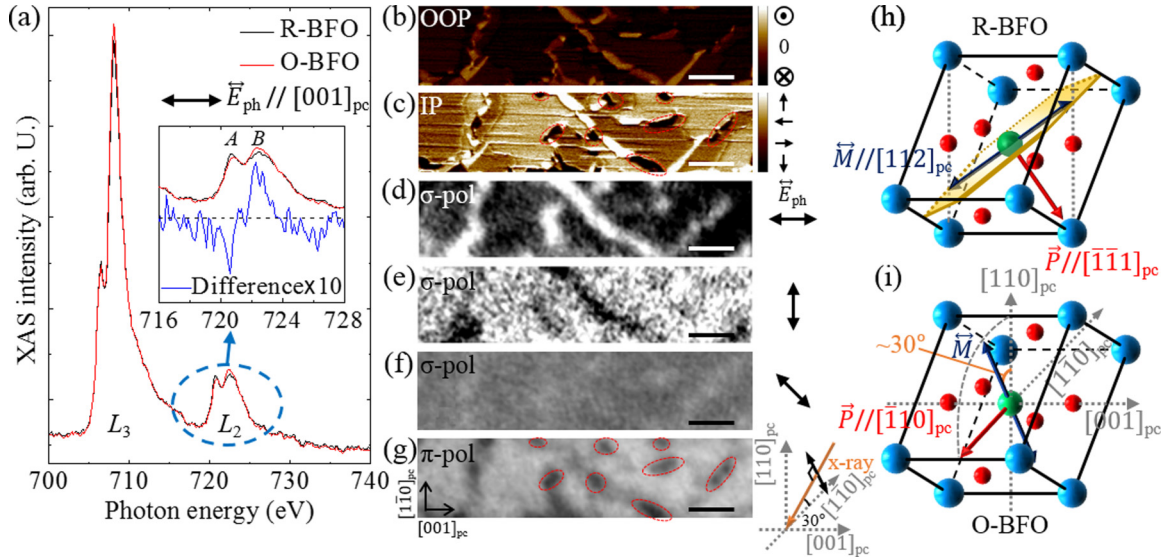
FIG. 4. (Color online) (a) XAS at Fe L edges with a σ-polarized x-ray beam where its electric field ($\vec{E}_{\mathrm{ph}}$) is aligned to $[001]_{\mathrm{pc}}$. In the inset, the enlarged L_2-edge spectra and their differences are presented. (b) OOP PFM image. (c) IP-PFM image. At the same region, a series of PEEM images were acquired by using linearly polarized x rays with the incident electric field along (d) $[001]_{\mathrm{pc}}$, (e) $[1\bar{1}0]_{\mathrm{pc}}$, (f) an in-plane axis rotated 45° from $[001]_{\mathrm{pc}}$, and (g) an axis 30° off from the surface normal. Contrast of the PEEM images represents the relative intensity of two L_2 subpeaks ($I_B - I_A$). Red dashed ovals indicating o^- domains in (c) and (g) are drawn to address the correlation between ferroelectric domains of O-BFO and their PEEM contrast with the π-polarized x ray. Scale bars represent 1 μm. Schematics on the right-hand side describe the ferroelectric polarization and the proposed magnetic easy axis of (h) R-BFO and (i) O-BFO. The spectra in (a) were obtained by means of microspectroscopy, i.e., integrating the intensities from two different domains in a stack of images.

A (I_A) at 721 eV] becomes relatively weaker (stronger) when $\vec{M}$ is more parallel to $\vec{E}_{\mathrm{ph}}$. Accordingly, we first consider the magnetic easy axis of R-BFO is more parallel to $[001]_{\mathrm{pc}}$ than that of O-BFO.

To address the antiferromagnetic axes, we employed PEEM because it provides a powerful tool to examine local electronic and magnetic structure at a spatial resolution of ~30 nm [29]. As shown in Figs. 4(b) and 4(c), the OOP and IP-PFM images identify positions of R-BFO and O-BFO phases clearly. We took PEEM images on the same area using three different linear x-ray σ polarizations at photon energies of 721 and 722.5 eV. The subtraction of the left L_2 peak intensity from the right one ($I_{\mathrm{PEEM}} = I_B - I_A$) becomes a good indicator to infer the magnetic easy axis. Corresponding PEEM images are shown in Figs. 4(d)–4(f). Indeed, we observe a clear difference in the local XAS spectra between O-BFO and R-BFO regions when x-ray polarization is along $[001]_{\mathrm{pc}}$ [Fig. 4(d)]. The needle-shaped O-BFO regions exhibit bright contrast as compared to the other R-BFO matrix area. It is seen that the contrasts become reversed when the linear polarization is rotated by 90° pointing to $[1\bar{1}0]_{\mathrm{pc}}$ [Fig. 4(e)]. However, we have observed little contrast for the image taken at linear polarization rotated by 45° with respect to $[001]_{\mathrm{pc}}$ [Fig. 4(f)]. Hence, these observations lead us to a presumption that the magnetic easy axis of R-BFO is more parallel to $[001]_{\mathrm{pc}}$ and that of O-BFO is along $[1\bar{1}0]_{\mathrm{pc}}$ in terms of their IP components.

However, this observation itself is not yet a full indication of their exact magnetic easy axes in three-dimensional space. For a better understanding, we performed an additional measurement of a PEEM image with π polarization as presented in Fig. 4(g). As compared with the IP-PFM image [Fig. 4(c)],

the PEEM image reveals that O-BFO regions have the domain-dependent contrast between o^- and o^+ domains. The contrast is due to magnetic origin because both domains share the same axis of ferroelectric polarization. This magnetic domain contrast cannot be distinguished if the magnetic easy axis of O-BFO is exactly parallel or perpendicular to the $[1\bar{1}0]_{\mathrm{pc}}$ axis. Therefore, the remaining high symmetric candidate for the magnetic easy axis of O-BFO allowing the domain-dependent contrast is an axis within a $(001)_{\mathrm{pc}}$ plane. The darker PEEM contrast in the o^- domains (marked by red dashed ovals in the figure) suggests that the magnetic easy axis of the o^- domain is closer to the x-ray polarization than that of the o^+ domain. On the other hand, the contrast of R-BFO domains is uniform regardless of their different IP polarizations, which indicates that the r_1^- and r_2^- domains are symmetric in the aspect of the interangle between their magnetic easy axis and the x-ray polarization. Combining all these observations, we propose the magnetic easy axis of R-BFO and O-BFO in our film to be as shown in Figs. 4(h) and 4(i).

This model of magnetic easy axes is consistent with the previous studies. It has been theoretically studied that the magnetic easy axis of bulk R-BFO lies within a $(111)_{\mathrm{pc}}$ plane perpendicular to its ferroelectric polarization [34]. The degeneracy within the plane can be lifted by a compressive monoclinic distortion. For example, growth of BFO on a $(001)_{\mathrm{pc}}$ SrTiO$_3$ substrate results in a magnetic easy axis along one of the in-plane $\langle 110 \rangle_{\mathrm{pc}}$ axes defined by an intersection of the $(111)_{\mathrm{pc}}$ magnetic easy plane and the $(001)_{\mathrm{pc}}$ film surface [35]. On the contrary, our film subject to the tensile strain on GSO substrate is expected to have the $\langle 112 \rangle_{\mathrm{pc}}$ axis as a magnetic easy axis of the tensile strained R-BFO. In addition, Yang *et al.* have reported that a tensile strained O-BFO film
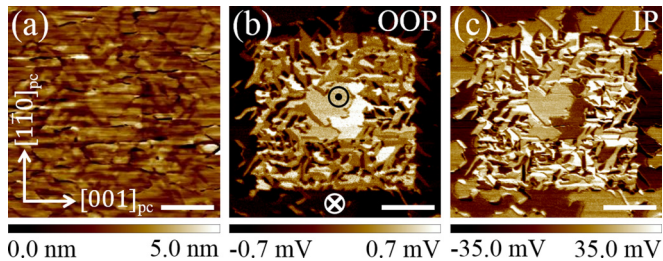
FIG. 5. (Color online) (a) Topographic image after the electric switching. (b) OOP PFM image which shows three different OOP ferroelectric polarization regions: as-grown R-O mixed BFO region, O-BFO dominant region with little OOP polarization (inside the outer box), and R-BFO dominant region with upward polarization (inside the inner box). (c) IP-PFM image of the same area. Scale bars indicate 2 μm.

has a magnetic easy axis tilted by 34° toward its ferroelectric polarization direction from the surface normal [22]. All these preceding reports support our results on the magnetic axes.

Finally, we explore the electric-field switching effect on the spatial distribution of O-BFO and R-BFO. As shown in Fig. 5, we applied electric fields by scanning with a conductive atomic force microscope tip biased at -3.5 V over the 6×6 μm^2 area, inside of which we made another poling box sized 2×2 μm^2 with a higher bias voltage of -10 V. Then we measured a PFM image over the whole double box area. Remarkably, we have found that the moderate strength electric field makes the O-BFO phase areas expand and their OOP PFM signal becomes nearly zero. On the other hand, strong electric poling reverses the OOP polarization to upward direction making the dominant phase R-BFO. As discussed before, the magnetic easy axes of these competing phases are perpendicular to each other in terms of IP components. Thus, the observation of electric-field-induced phase switching offers an opportunity for magnetoelectric applications.

The magnetoelectric coupling of R-BFO has been demonstrated in the form of electrical switching of the magnetic plane [35]. But the lack of net magnetization in BFO demands hybrid structures consisting of BFO and other ferromagnetic layers such as CoFe [36–38], $La_{0.7}Sr_{0.3}MnO_3$ [39,40], and permalloy [41]. In these magnetoelectric devices, an external electric field switches the magnetic easy axis of BFO and the switching is delivered to adjacent ferromagnetic layers through exchange coupling/bias. However, the rotation of magnetic plane in R-BFO is always accompanied by ferroelastic switching, which is unstable in terms of elastic energy since the switched region deforms elastically against other surrounding areas. Instead, it is more favorable that other elastically compatible ferroelectric states emerge via 180° domain switching by holding the magnetic easy axis as it is. Thus, reliable ferroelastic switching has been a critical issue for realizing magnetoelectric devices of BFO [42]. Our current observation regarding the magnetic axis rotation provides an ideal pathway to magnetoelectric applications due to the fact that the application of an external electric field compels the resultant state in a deterministic way without other undesirable paths of switching.

In summary, we observed phase separation of R-BFO and O-BFO phases in epitaxial BFO films grown on $(110)_{pc}$-oriented GSO substrates, which provides a tensile misfit strain. We characterized PFM domain structure, strain state, and magnetic easy axis for each phase and explored electric-field-induced phase switching. The discovery of phase separation between R-BFO and O-BFO and their electrical controllability not only reveals thought-provoking fundamental issues regarding phase competition but also offers a promising pathway to the electrical rotation of a magnetic axis.

[1] W. Eerenstein, N. D. Mathur, and J. F. Scott, Nature (London) **442**, 759 (2006).

[2] S.-W. Cheong and M. Mostovoy, Nat. Mater. **6**, 13 (2007).

[3] R. Ramesh and N. A. Spaldin, Nat. Mater. **6**, 21 (2007).

[4] Y. Tokura, J. Magn. Magn. Mater. **310**, 1145 (2007).

[5] D. Khomskii, Physics **2**, 20 (2009).

[6] F. Kubel and H. Schmid, Acta Crystallogr., Sect. B: Struct. Sci. **46**, 698 (1990).

[7] D. Lebeugle, D. Colson, A. Forget, and M. Viret, Appl. Phys. Lett. **91**, 022907 (2007).

[8] J. Wang, J. B. Neaton, H. Zheng, V. Nagarajan, S. B. Ogale, B. Liu, D. Viehland, V. Vaithyanathan, D. G. Schlom, U. V. Waghmare, N. A. Spaldin, K. M. Rabe, M. Wuttig, and R. Ramesh, Science **299**, 1719 (2003).

[9] L. W. Martin, S. P. Crane, Y.-H. Chu, M. B. Holcomb, M. Gajek, M. Huijben, C.-H. Yang, N. Balke, and R. Ramesh, J. Phys.: Condens. Matter **20**, 434220 (2008).

[10] Y. L. Li, S. Y. Hu, Z. K. Liu, and L. Q. Chen, Acta. Mater. **50**, 395 (2002).

[11] J. X. Zhang, D. G. Schlom, L. Q. Chen, and C. B. Eom, Appl. Phys. Lett. **95**, 122904 (2009).

[12] H. Béa, B. Dupé, S. Fusil, R. Mattana, E. Jacquet, B. Warot-Fonrose, F. Wilhelm, A. Rogalev, S. Petit, V. Cros, A. Anane, F. Petroff, K. Bouzehouane, G. Geneste, B. Dkhil, S. Lisenkov, I. Ponomareva, L. Bellaiche, M. Bibes, and A. Barthélémy, Phys. Rev. Lett. **102**, 217603 (2009).

[13] R. J. Zeches, M. D. Rossell, J. X. Zhang, A. J. Hatt, Q. He, C.-H. Yang, A. Kumar, C. H. Wang, A. Melville, C. Adamo, G. Sheng, Y.-H. Chu, J. F. Ihlefeld, R. Erni, C. Ederer, V. Gopalan, L. Q. Chen, D. G. Schlom, N. A. Spaldin, L. W. Martin, and R. Ramesh, Science **326**, 977 (2009).

[14] A. J. Hatt, N. A. Spaldin, and C. Ederer, Phys. Rev. B **81**, 054109 (2010).

[15] H. M. Christen, J. H. Nam, H. S. Kim, A. J. Hatt, and N. A. Spaldin, Phys. Rev. B **83**, 144107 (2011).

[16] Z. Chen, S. Prosandeev, Z. L. Luo, W. Ren, Y. Qi, C. W. Huang, L. You, C. Gao, I. A. Kornev, T. Wu, J. Wang, P. Yang, T. Sritharan, L. Bellaiche, and L. Chen, Phys. Rev. B **84**, 094116 (2011).

[17] K.-T. Ko, M. H. Jung, Q. He, J. H. Lee, C. S. Woo, K. Chu, J. Seidel, B.-G. Jeon, Y. S. Oh, K. H. Kim, W.-I. Liang, H.-J. Chen, Y.-H. Chu, Y. H. Jeong, R. Ramesh, J.-H. Park, and C.-H. Yang, Nat. Commun. **2**, 567 (2011).

[18] K.-Y. Choi, S. H. Do, P. Lemmens, D. Wulferding, C. S. Woo, J. H. Lee, K. Chu, and C.-H. Yang, Phys. Rev. B **84**, 132408 (2011).

[19] C.-S. Woo, J. H. Lee, K. Chu, B.-K. Jang, Y.-B. Kim, T. Y. Koo, P. Yang, Y. Qi, Z. Chen, L. Chen, H. C. Choi, J. H. Shim, and C.-H. Yang, Phys. Rev. B **86**, 054417 (2012).

[20] B. Dupé, S. Prosandeev, G. Geneste, B. Dkhil, and L. Bellaiche, Phys. Rev. Lett. **106**, 237601 (2011).

[21] Y. Yang, W. Ren, M. Stengel, X. H. Yan, and L. Bellaiche, Phys. Rev. Lett. **109**, 057602 (2012).

[22] J. C. Yang, Q. He, S. J. Suresha, C. Y. Kuo, C. Y. Peng, R. C. Haislmaier, M. A. Motyka, G. Sheng, C. Adamo, H. J. Lin, Z. Hu, L. Chang, L. H. Tjeng, E. Arenholz, N. J. Podraza, M. Bernhagen, R. Uecker, D. G. Schlom, V. Gopalan, L. Q. Chen, C. T. Chen, R. Ramesh, and Y. H. Chu, Phys. Rev. Lett. **109**, 247606 (2012).

[23] J. X. Zhang, B. Xiang, Q. He, J. Seidel, R. J. Zeches, P. Yu, S. Y. Yang, C. H. Wang, Y.-H. Chu, L. W. Martin, A. M. Minor, and R. Ramesh, Nat. Nanotechnol. **6**, 98 (2011).

[24] A. R. Damodaran, C.-W. Liang, Q. He, C.-Y. Peng, L. Chang, Y.-H. Chu, and L. W. Martin, Adv. Mater. **23**, 3170 (2011).

[25] Q. He, Y.-H. Chu, J. T. Heron, S. Y. Yang, W. I. Liang, C. Y. Kuo, H. J. Lin, P. Yu, C. W. Liang, R. J. Zeches, W. C. Kuo, J. Y. Juang, C. T. Chen, E. Arenholz, A. Scholl, and R. Ramesh, Nat. Commun. **2**, 225 (2011).

[26] K.-E. Kim, B.-K. Jang, Y. Heo, J. H. Lee, M. Jeong, J. Y. Lee, J. Seidel, and C.-H. Yang, NPG Asia Mater. **6**, e81 (2014).

[27] I. C. Infante, S. Lisenkov, B. Dupé, M. Bibes, S. Fusil, E. Jacquet, G. Geneste, S. Petit, A. Courtial, J. Juraszek, L. Bellaiche, A. Barthélémy, and B. Dkhil, Phys. Rev. Lett. **105**, 057601 (2010).

[28] R. Uecker, D. Klimm, R. Bertram, M. Bernhagen, I. Schulze-Jonack, M. Brützam, A. Kwasniewski, Th. M. Gesing, and D. G. Schlom, Acta Phys. Pol. A **124**, 295 (2013).

[29] F. Kronast, J. Schlichting, F. Radu, S. K. Mishra, T. Noll, and H. A. Dürr, Surf. Interface Anal. **42**, 1532 (2010).

[30] Y.-H. Chu, M. P. Cruz, C.-H. Yang, L. W. Martin, P.-L. Yang, J.-X. Zhang, K. Lee, P. Yu, L.-Q. Chen, and R. Ramesh, Adv. Mater. **19**, 2662 (2007).

[31] C.-H. Yang, D. Kan, I. Takeuchi, V. Nagarajan, and J. Seidel, Phys. Chem. Chem. Phys. **14**, 15953 (2012).

[32] J. Lüning, F. Nolting, A. Scholl, H. Ohldag, J. W. Seo, J. Fompeyrine, J.-P. Locquet, and J. Stöhr, Phys. Rev. B **67**, 214433 (2003).

[33] E. Arenholz, G. van der Laan, R. V. Chopdekar, and Y. Suzuki, Phys. Rev. B **74**, 094407 (2006).

[34] C. Ederer and N. A. Spaldin, Phys. Rev. B **71**, 060401 (2005).

[35] T. Zhao, A. Scholl, F. Zavaliche, K. Lee, M. Barry, A. Doran, M. P. Cruz, Y. H. Chu, C. Ederer, N. A. Spaldin, R. R. Das, D. M. Kim, S. H. Baek, C. B. Eom, and R. Ramesh, Nat. Mater. **5**, 823 (2006).

[36] Y.-H. Chu, L. W. Martin, M. B. Holcomb, M. Gajek, S.-J. Han, Q. He, N. Balke, C.-H. Yang, D. Lee, W. Hu, Q. Zhan, P.-L. Yang, A. Fraile-Rodríguez, A. Scholl, S. X. Wang, and R. Ramesh, Nat. Mater. **7**, 478 (2008).

[37] J. T. Heron, M. Trassin, K. Ashraf, M. Gajek, Q. He, S. Y. Yang, D. E. Nikonov, Y.-H. Chu, S. Salahuddin, and R. Ramesh, Phys. Rev. Lett. **107**, 217202 (2011).

[38] M. Trassin, J. D. Clarkson, S. R. Bowden, J. Liu, J. T. Heron, R. J. Paull, E. Arenholz, D. T. Pierce, and J. Unguris, Phys. Rev. B **87**, 134426 (2013).

[39] P. Yu, J.-S. Lee, S. Okamoto, M. D. Rossell, M. Huijben, C.-H. Yang, Q. He, J. X. Zhang, S. Y. Yang, M. J. Lee, Q. M. Ramasse, R. Erni, Y.-H. Chu, D. A. Arena, C.-C. Kao, L. W. Martin, and R. Ramesh, Phys. Rev. Lett. **105**, 027201 (2010).

[40] S. M. Wu, S. A. Cybart, D. Yi, J. M. Parker, R. Ramesh, and R. C. Dynes, Phys. Rev. Lett. **110**, 067202 (2013).

[41] D. Lebeugle, A. Mougin, M. Viret, D. Colson, and L. Ranno, Phys. Rev. Lett. **103**, 257601 (2009).

[42] S. H. Baek, H. W. Jang, C. M. Folkman, Y. L. Li, B. Winchester, J. X. Zhang, Q. He, Y. H. Chu, C. T. Nelson, M. S. Rzchowski, X. Q. Pan, R. Ramesh, L. Q. Chen, and C. B. Eom, Nat. Mater. **9**, 309 (2010).